

Virus-Templated Near-Amorphous Iron Oxide Nanotubes

Sachin N. Shah,^{†,‡,■} Abid A. Khan,^{†,#} Ana Espinosa,[§] Miguel A. Garcia,^Δ Wiwat Nuansing,[†] Mariana Ungureanu,[○] Jonathan G. Heddle,^{‡,¶} Andrey L. Chuvilin,^{†,◆} Christina Wege,[¶] and Alexander M. Bittner*^{†,◆}

[†]CIC nanoGUNE Consolider, E-20018, Donostia-San Sebastián, Spain

[‡]Heddle IRU, RIKEN, 2-1 Hirosawa, Wako, Saitama 351-0198, Japan

[¶]Malopolska Centre of Biotechnology, Jagiellonian University, Gronostajowa 7, 30–387, Krakow, Poland

[■]Department of Chemistry, University of Hull, HU6 7RX, Hull, United Kingdom

[#]Department of Biosciences, COMSATS Institute of Information Technology, Park Road, Chak Shehzad, 44000 Islamabad, Pakistan

[§]Instituto de Ciencia de Materiales de Madrid (ICMM) Consejo Superior de Investigaciones Científicas, c/ Sor Juana Inés de la Cruz 3, Cantoblanco, 28049, Madrid, Spain

^ΔInstituto de Ceramica y Vidrio - CSIC, and Instituto de Magnetismo Aplicado “Salvador Velayos” UCM_ADIF, 28049, Madrid, Spain

[○]CIC biomaGUNE, E-20009, Donostia-San Sebastián, Spain

[◆]Ikerbasque, Basque Foundation for Science, E-48013, Bilbao, Spain

¶University of Stuttgart, Institute of Biomaterials and Biomolecular Systems,
Pfaffenwaldring 57, D-70569 Stuttgart, Germany

E-mail: a.bittner@nanogune.eu

ABSTRACT

We present a simple synthesis of iron oxide nanotubes, grown under very mild conditions from a solution containing Fe(II) and Fe(III), on rod-shaped tobacco mosaic virus templates. Their well-defined shape and surface chemistry suggest that these robust bionanoparticles are a versatile platform for synthesis of small, thin mineral tubes, which was achieved efficiently. Various characterization tools were used to explore the iron oxide in detail: Electron microscopy (SEM, TEM), magnetometry (SQUID-VSM), diffraction (XRD, TEM-SAED), electron spectroscopies (EELS, EDX, XPS), and X-ray absorption (XANES with EXAFS analysis). They allowed determination of the structure, crystallinity, magnetic properties, and composition of the tubes. The protein surface of the viral templates was crucial to nucleate iron oxide, exhibiting analogies to biomineralization in natural compartments such as ferritin cages.

INTRODUCTION

Iron oxide biomineralization is of substantial importance in natural systems. Best-known examples are the storage of iron as ferrihydrite inside ferritin cages, the synthesis of magnetite in magnetotactic bacteria, and the presence of iron oxide in birds.¹⁻⁴ Morphology and structure of the inorganic deposits are usually the focus of interest, in conjunction with the chemical and biochemical reactions that produce the oxide under

ambient conditions. In the case of cage-like templates, the interface between iron oxide and its biological environment is considered more in the context of functionalization of the produced particles, and less in the context of templating, i.e., for the case that a prefabricated structure imposes its geometry on the iron oxide. A better modulation, and potentially understanding, of the mineralization may be achieved when the templating substrate is both structurally and chemically well-defined, conditions that are not easily met inside protein nanocontainers. This is why we decided to employ the external surface (the protein capsid) of the 18 nm wide tobacco mosaic virus (TMV) as a scaffolding platform. This tobamovirus is stable up to pH 9, and, although it is built from RNA and proteins only, mechanically it is surprisingly rigid. TMV offers a well-known helical arrangement of 2130 coat protein (CP) subunits enclosing a single RNA strand, and an internal channel of 4 nm diameter. The axial protein–protein distance is given by the helix pitch of 2.3 nm, and the tangential distance is 3.5 nm (49 proteins correspond to three helical turns). Each of these 2.3 nm × 3.5 nm patches of the CP subunits exposes the rather flexible amino- and carboxylate termini of the protein, with the N-terminal amino group of Ser-1 acetylated, and the α amine of Trp-152 in the vicinity of the C-terminus carrying a carboxylate group and five hydroxyl groups [i.e., side chains of two serine residues 3 and 154 (not visible in pdb 2TMV) and a third additional Ser-155 present in the TMV clone used (see Supporting Information); and two threonine side chains of Thr-153 and Thr-158 (not visible in fiber diffraction studies)] (Figure 1 a). In summary, this provides a template with a large number of potential ligands for Fe(II) and Fe(III), in a regular and defined repetitive arrangement. We were inspired by results

obtained with this surface, for binding particles,⁵⁻¹¹ or depositing metal layers,^{8,12-14} and for growing oxides.¹⁵⁻¹⁷ i.e., iron oxide on tobamoviruses.^{17,18}

While syntheses for nanoparticles of iron oxides are well established,¹⁹ nanorods and especially nanotubes are less explored,²⁰⁻²⁸ although they may show unusual magnetic properties.^{12,28} Nanotubes could be an important alternative to the usual spherical nanoparticles in medical applications,²⁹⁻³² and if hollow, spherical iron oxide nanoparticles have proven beneficial for magnetic resonance imaging³³ and therapeutic hyperthermia.³⁴ Here iron oxides are of utmost importance due to their unique combination of nontoxicity and room temperature (ferri)magnetism. Another possible application might be drug delivery from the internal cavity of nanotubes (in our case, from the internal channel of TMV), which is still an underdeveloped research area. In this scenario, the tubular template incorporates the drug, but also exposes functional groups to bind the iron oxide on its external surface. For this application, smaller tubes might be preferable to be incorporated into living cells.

Iron oxide layers grown from solution show a range of magnetic properties that depend on both structure and size (layer thickness) of the samples.³⁴⁻³⁷ The most beautiful examples are found in natural nanomagnets (e.g., in birds).¹ Note that usually only the two ferrimagnetic oxides Fe_3O_4 (magnetite) and $\gamma\text{-Fe}_2\text{O}_3$ (maghemite) can have nonzero magnetic moments at 300 K (some other oxides and hydroxides can show similar, but very weak effects).² However, below 10 nm for $\gamma\text{-Fe}_2\text{O}_3$, and below 6 nm for Fe_3O_4 ,² spherical nanoparticles become superparamagnetic, and magnetic moments can build up only in the presence of external fields. A similar phenomenon is also known for

larger particles in suspension, due to random orientation (the magnetic moments are in this case locked to the nanoparticle geometry, but the particles tumble in the liquid). The behavior of nanoscale rods and tubes is different from that of spheres; generally, the anisotropic shape modifies the coercivity, which, however, also depends on crystallinity and composition.²⁰⁻²⁸

In our study, a 1:2 mixture of aqueous Fe(II) and Fe(III) salts was employed for mineral deposition under mild reaction conditions, in order to produce Fe₃O₄ (=Fe(II)Fe(III)₂O₄). We did, however, not *a priori* exclude the presence of other iron oxides, which can influence many physical properties. We optimized the synthesis conditions to obtain a very thin, but continuous coating on TMV. The natural diameter of TMV (18 nm) determines the inner diameter of the iron oxide tube, while the outer diameter of the resulting bioinorganic hybrid depends on the synthesis conditions. Product characterization was carried out by a multimethod analysis based on electron microscopy (SEM, TEM), magnetometry (SQUID-VSM), diffraction (XRD, TEM-SAED), electron spectroscopies (EELS, EDX, XPS), and X-ray absorption (XANES with EXAFS analysis).

RESULTS AND DISCUSSION

Our synthesis is based on mixing TMV with Fe(II) and Fe(III) at slightly elevated pH in aqueous suspension and incubation for 10 min at room temperature (23°C). After careful purification by centrifugation and dialysis, we obtained a brown suspension (see Experimental Section). Upon drying of a droplet of the suspension on a substrate, we acquired electron microscopy (EM) images (Figure 1). Scanning EM (SEM) shows

individual, coated TMV rods (light gray) on the dark gray wafer background, while untreated TMV appears darker than the background due to the reduced amount of secondary electrons emitted from uncoated rods (at low imaging voltages). Transmission EM (TEM) (Figure 1 b) shows rod diameters around 35 nm, while untreated TMV measures only 18 nm (see Supporting Information, Figure S1 and S2). The average rod length appears substantially larger than the 300 nm of a single natural virus particle (virion). This may be attributed to linear aggregation of the TMV rods, which is well-known for virus suspensions, even in the absence of inorganic deposits.³⁸ We thus can conclude that under the conditions applied, TMV becomes coated with a layer of ≈ 9 nm of material. Given the synthesis in aqueous suspension, the material has to contain at least iron and oxygen (see verification below). It is not arranged in rods, but in tubes; the TEM data exclude any penetration into the biological template: The outer rim strictly follows the viral shape (rod-like), hence the virions are still present as cores inside the composite objects. The affinity of iron for oxygen and especially for OH groups is the base for a possible mechanism underlying the mineralization reaction: The large number of OH groups (eight should be accessible on a single protein, so ≈ 17000 per virion) means that the first Fe(II) and Fe(III) ions that encounter the virion bind here. Since the ions themselves expose OH groups in their first ligand shell, they then act as nuclei for a further attachment of Fe(II) and Fe(III), and a layer of iron hydroxides grows. The elimination of water will then produce oxides or mixed hydroxides/oxides (see below). From our images we cannot deduce meaningful information on a possible mineralization of the internal 4 nm wide channel of TMV, which might be filled to a nonpredictable

extent with other ferromagnetic metals.^{8, 39, 40} Even a complete filling would, however, at best amount to <2 % of the coating.

In contrast to the rather smooth layer grown on each individual TMV, the aggregation of the rods during the process is less well controlled: The precipitating oxide may bind to all external surfaces of TMV available in its vicinity. In this way, two virions that come in contact accidentally may quickly “cement” into a stable junction, ultimately yielding an irregular network of mineralized TMV (Figure 1 b), as has been observed in previous studies on other inorganic deposits.⁴¹ This means that within the suspension of nascent hybrid tubes, no significant movement of individual TMVs occurred. However, each single virion remained accessible to ions, and was completely mineralized (Figure 1 c,d). The final coating is sufficiently thick to be studied by energy dispersive X-ray spectroscopy (EDX) even on single rods (Figure 1d). This spectrum, as well as spectra from larger networks of mineralized TMV, confirms the presence of iron in the layer. Since all iron had been in contact with water (and oxygen), we infer the presence of iron oxide(s) and/or iron hydroxide(s) from our EDX results (confirmed by the other spectroscopic techniques, see below). Although the oxygen/carbon ratio determined from spots focused on single mineralized virions was above that from bare sample areas (see Supporting Information, Figure S3), the presence of oxygen could not be quantified since the virion, the substrate, and the background already provided very high oxygen signals. Moreover, the carbon detected by EDX is partially from the very small amounts of residual gas (contamination) that have reacted in the electron beam. We also found silicon (sample substrate) and traces of sodium and chlorine (from traces of the educt

FeCl₃ and the product NaCl). We found no other elements, and can thus exclude large amounts (% range) of impurities.

Our TEM data reveal product diameters of ≈ 35 nm, in agreement with the SEM results. The virus particles were imaged with a diameter of 15 nm, and were coated with a ≈ 9 nm thick shell, containing material of higher electron absorption (Figure 1 b). We observed a sharp and straight TMV/iron oxide interface, which suggests an intact outer surface of the virion, as expected from the suggested scenario of hydroxyl groups acting as ligands. We can compare this to the inverse case of proteins, which directly bind to iron oxide particles. Mehta et al.⁴² prepared their systems in a similar way to our synthesis and found that, analogous to the TMV capsid, albumin and various enzymes largely retain their structure and function when they contact iron oxides. The well-preserved shape of the TMV is a clear advantage of our low-temperature method; for example, above 90 °C, one would expect complete loss of the tubular structure.⁴³

The shell of deposited material is not completely homogeneous, but oscillates in thickness, at distances of ≈ 20 nm, hence the surface appears rippled (see Figure 1). In principle, this could point to a mineralization mechanism based at least partially on the attachment of preformed particles (homogeneous nucleation). We found, however, that the oxide nucleates heterogeneously: We tested a “post mineralization” scenario, i.e., synthesis of iron oxide in the absence of TMV, but under similar conditions, followed by adding the virus (Figure 2). We employed the chemically very similar tomato mosaic virus (ToMV; see Supporting Information Figure S4, S5, and S6). After our careful purification procedure (see Experimental Section), we detected only a very small amount

of iron oxide on ToMV for the "post mineralization". Already prepared iron oxide particles do not bind well to TMV, in contrast to Fe(II) and Fe(III), which attach readily. As mentioned in the Introduction, this is due to a regular and defined repetitive arrangement of hydroxyl groups, which is identical on TMV and ToMV.

Closer inspection of Figure 1 b shows that the material is composed of very small particles (<5 nm), which are closely interconnected. These particles exhibit no substructure. The same result was obtained in the absence of TMV (see also Supporting Information Figure S7), and similar scenarios are known for iron oxide mineralization in nature.⁴⁴ We conclude that TMV acts solely as a nucleation seed, but does not induce any preferential orientation or structure in the material. This is in striking contrast to biochemical mineralization, which in most cases gives crystals, in some cases even nearly perfect spinel phases.² Heterogeneous nucleation would indeed suggest that a part of the material grows very fast at some favored locations (oxygen-containing groups).⁴⁵ Coalescence can then induce an incomplete smoothing, and hence a ripple-like appearance. Focusing on the atomic scale, the arrangement of hydroxyl groups on tobamoviruses does not fit to the structure of any crystal face, hence heteroepitactic growth would not be possible. In addition, natural mineralization processes are typically much slower than our precipitation reaction, giving the ions time and catalytic pathways (based on protein domains, peptides or in some cases enzymes, which may also rely on further supplementary compounds), to arrange in a crystalline structure.

Further detailed analysis requires diffraction methods such as powder X-ray diffraction (XRD) (Figure 3). As a standard, we employed Fe₃O₄, (Figure 3 a; we also

use the Fe_3O_4 assignment for the peaks). The signals fit to Fe_3O_4 and would equally well fit to $\gamma\text{-Fe}_2\text{O}_3$, but not to other oxides; note that the defective spinel structure (and thus the diffractogram) of $\gamma\text{-Fe}_2\text{O}_3$ is very similar to the perfect spinel structure of Fe_3O_4 . Mineralized TMV yields a nearly featureless diffractogram (Figure 3 b). This corresponds well to most reports on amorphous iron oxide.⁴⁶⁻⁴⁸ However, close inspection shows two maxima (very broad peaks) at positions that correspond to (311) and (440), where the diffraction intensity is very high in Fe_3O_4 . In order to exclude problems of the experimental setup or of the amount of material, the sample (Figure 3 b) was obtained from slightly more material than the standard (Figure 3 a). Signal/noise considerations suggest that at best 13% of the sample can be in a well-crystallized form (Supporting Information, estimation of the fraction of crystalline material). Further details are provided by selected area electron diffraction (SAED) in TEM, which exhibited no spots, merely diffuse rings. The maxima (Figure 3 c, Supporting Information Figure S8) are located at (311), (400), (511), and (440), compatible with the XRD results. The peak width suggests that any crystallites must be smaller than two unit cells, so the structure is “nearly amorphous”. We use this term to express that there is some local order, compatible with spinel structures, also found for oxidized nanoparticles.⁴⁹ By using XRD and SAED we have confirmed this for macroscopic samples, and additionally on the nanoscale.

Amorphous structures often transform into crystalline phases upon thermal treatment. Our near-amorphous samples showed no changes in size or shape upon heating (tested by SEM). Thermal treatment in vacuum (at 570 K) and in air (at 520 K) produced the expected crystalline phase(s) (Figure 3 d and 3 e). These diffraction data do not fit to

α -Fe₂O₃, but they fit well to γ -Fe₂O₃ and also to Fe₃O₄, which we do not distinguish with our diffraction method. Heating in air to below 600 K is known to cause complete oxidation to γ -Fe₂O₃, while vacuum prevents oxidation, and should thus conserve our educt composition, e.g., as Fe₃O₄. Our results agree with literature reports on thermal treatment of Fe(II) oxides.^{47, 50–52} In passing we note that such high temperatures ensure that TMV is totally carbonized or oxidized. Additional peaks, present already in the unheated samples, correspond to NaCl from the educts in our synthesis. However, it is not clear why the signal/noise ratios (peak intensities compared to the noise level) differ between the annealed samples and the unheated sample (no NaCl found). SAED found no NaCl either, hence any NaCl is located at considerable distance from the virions, and not in contact with the iron oxide.

We analyzed the magnetic properties of dried droplets of our nanotube suspension with a SQUID-VSM (Superconducting Quantum Interference Device with Vibrating Sample Magnetometer head).⁵³ We checked that there was no magnetic signal coming from the sample holder, or contamination that could override the small signals from our samples. We carefully purified our samples (see Experimental Section), removing all larger objects (such as micrometer-sized iron oxide crystals), and verified this with SEM. Figure 4 shows magnetization curves recorded at 300 K and at 5 K; the low temperature resulted in a higher value of saturation magnetization. Our saturation magnetization of 0.0008 emu/g (0.0008 Am²/kg) at 300 K is extremely small, and correlates well with amorphous iron oxide phases produced by other methods.^{2,46} (see more details in the Supporting Information, SQUID–VSM Magnetometry of small amount of weakly magnetic sample).

It is possible that the saturation magnetization is undetectable, and that all measured magnetization results from a very small amount of crystalline ferro/ferrimagnets of high magnetic moment. Most likely candidates are trace amounts of the spinel phases γ -Fe₂O₃ or Fe₃O₄, which may have escaped the detection by electron microscopy and diffraction. They are in fact the only iron oxides with high magnetic bulk moments, 76 emu/g for γ -Fe₂O₃,^{54, 55} and \approx 92 emu/g for Fe₃O₄.⁵⁵ Similar values are found for crystalline iron oxide tubes and rods.⁵⁶⁻⁶⁰ Zhou et. al.⁶⁰ obtained a value of 106 emu/g for γ -Fe₂O₃ nanorods, and Geng et.al.⁵⁹ report 82 emu/g for Fe₃O₄ nanotubes, both of larger size than our tubes. We exclude the very small intrinsically present magnetic moment in other oxide phases (some antiferromagnetic oxides, e.g., α -Fe₂O₃, can carry a small ferrimagnetic moment) because in this case a considerable fraction of our material would have to be in this form, thus showing up in the analytical data.

Linear structures are known to exhibit shape anisotropy. This effect is based on the alignment of the spins parallel to the principal axis: Higher energies are required to reverse them, which translates into increased magnetic coercivities.⁶¹ Shape anisotropy persists even for completely amorphous materials,^{62, 63} which explains the observation of a hysteresis (Figure 4). Our coercive field of 0.04 T (400 Oe) at 300 K is higher than the values reported for bulk iron oxides and nanoparticles, e.g., 0.03 T for bulk γ -Fe₂O₃,⁶⁰ 0.008 T for γ -Fe₂O₃ nanorods,⁶⁴ \approx 0.013 T for bulk Fe₃O₄,⁶⁵ 0.017 T for Fe₃O₄ nanotubes.⁵⁹ Our observation is not consistent with the above-mentioned very small amount of spinel(s). Hence we suggest that our near-amorphous oxide is weakly ferro/ferrimagnetic, and that it shows considerable anisotropy due to the elongated shape.

For the observed average thickness of 9 nm, a single virion of 300 nm length and 18 nm diameter can accommodate not more than 1.2×10^{-15} g of Fe_3O_4 (bulk density 5.17 g/cm^3). This would translate into only 10^{-18} emu per tube, which is not sufficient to align the tubes in a magnetic field during synthesis. However, larger networks of virions, with sizes well above micrometers, can align in fields, and move in field gradients (see Supporting Information for alignment test in external magnetic field and Figures S9, S10, S11 and S12). Only upon annealing did we observe sizable moments, based on forming crystalline material (Figure 5): the saturation magnetization increased to $>1 \text{ emu/g}$ ($>1 \text{ Am}^2/\text{kg}$), while the coercivity reduced to $\approx 0.001 \text{ T}$. The values now fit well to typical crystalline and nanoscale iron oxides.^{2,46}

The structural and the magnetometry data suggest a weakly ferro- or ferrimagnetic layer of near-amorphous iron oxide. In order to elucidate the oxidation state and chemical properties, we extended our analyses to XPS and EELS (Figure 6). The techniques rely on analyzing the energy of emitted electrons, and on the energy loss of transmitted electrons, respectively, in both cases via excitations at the iron L edge, hence the spectra are generally very similar. We recorded EELS using TEM, by analyzing the energy of the inelastically scattered electrons, and compared our samples to various iron oxide standards. The XPS data, which are rather noisy, were recorded from a very small sample mass and nonpurified samples yielded clearer spectra with identical features, (see Supporting Information, Figure S13. XPS and EELS allow a thorough analysis: In addition to the detailed scans in the iron region (see below), we found the standard peaks for carbon at 284.8 eV, nitrogen at 400.0 eV, and a trace of phosphorus at 133.2 eV, which can all be assigned to TMV. Residues of NaCl from the educt solution resulted in

signals for Na^+ at 1070.7 eV and for Cl^- at 199.6 eV (not found in EELS since the TEM beam was focused to the virions, while NaCl was not found adjacent or bound to TMV). Oxygen yielded additional peaks, stemming from TMV and iron oxide, which were less useful for the analysis in our case.

Figure 6 shows slightly different peak shapes for XPS and EELS, suggesting a shift, which could result from the zero loss drift in EELS. Otherwise the differences between various forms of iron oxide are minimal in either technique. Correct peak fitting is crucially important for XPS: We observe four peaks, of which two are asymmetric, hence we require at least six fit components. The first four components are due to the splitting of each of the Fe 2p features (3/2 and 1/2) into two peaks. Our XPS fitting result is 710.3 and 713.3 eV for Fe 2p_{3/2}, and 723.7 and 726.6 eV for Fe 2p_{1/2} (for accuracy and details, see Supporting Information, Figure S13). This is compatible with a mixture of Fe(III) and Fe(II) as in Fe_3O_4 , although with slightly elevated binding energies for Fe(II).^{2,66} The fifth and sixth component are required to account for the weak features at 718.6 eV and at 730.2 eV, which are shakeup satellite signals, as discussed in detail elsewhere.⁶⁷⁻⁶⁹ They are typical of Fe(III); the Fe(II) shakeup processes cause even weaker signals. The quantitative evaluation of relative amounts of iron oxides is very difficult even when the shake-up features are included, as already pointed out by Lin et al.⁶⁷

Our EELS results exhibit much less noise, and allowed for quantification. To this end, we added the spectra taken from the $\gamma\text{-Fe}_2\text{O}_3$ and Fe_3O_4 standards, taken under identical conditions, in varying ratios (Supporting Information Figure S14 and S15). For

a ratio of 2 mol γ -Fe₂O₃ to 1 mol of FeO, the sum (Figure S14) fits very nicely to the recorded spectrum (Figure 6). We thus produced material that contains both Fe(II) and Fe(III), and that is, concerning the oxidation state of the iron atoms, “chemically” similar to Fe₃O₄ (but of course near-amorphous).⁴⁹ The peaks at 709.2 eV (shoulder), 711.1, 722.7, and 724.5 eV, and the shakeup signal 718.1 eV compare well with the XPS results, though slightly shifted to lower energies, as mentioned above.

In order to determine the direct environment and local geometry of the iron atoms, we resorted to X-ray absorption near-edge spectroscopy (XANES) at the K edge, again from samples dried on silicon wafers. Figure 7a shows spectra for the sample and various references (metallic Fe, FeO, α -Fe₂O₃, γ -Fe₂O₃ and Fe₃O₄), recorded under identical conditions (see Experiment Section). A detail of the K edge region is shown in Figure 7 b. We found that both mineralized TMV samples (as-grown and annealed) present the same edge position, defined as the point of maximum slope, as γ -Fe₂O₃ and α -Fe₂O₃, hence Fe(III) is the dominant oxidation state. As discussed above, XRD measurements of the air annealed sample do not support the presence of α -Fe₂O₃, so we can rule out the existence of a detectable fraction of this oxide. We found the pre-edge region (for details, see Figure 7 c) especially useful: Iron oxides show a peak here associated mainly with noncentrosymmetric (tetrahedral) positions. These positions are occupied by Fe(III) in the case of the spinels γ -Fe₂O₃ and Fe₃O₄⁷⁰ (in the case of α -Fe₂O₃, Fe(III) would be located exclusively in octahedral sites, with a very diminished pre-edge peak). The pre-edge peak in our samples was located at the same position as that of the references Fe₃O₄ and γ -Fe₂O₃, but slightly less pronounced. Since we rule out α -Fe₂O₃ from our XRD data, the data suggest that our samples contain iron atoms in tetrahedral and also in

octahedral sites, as indeed present in the spinels. This local symmetry does not suggest any translational symmetry, and is fully compatible with our near-amorphous structure.

The interface between the virus surface and the first layer of iron oxide can be of different symmetry and even oxidation state, but the amount of iron atoms is too small to be detected. Furthermore we cannot rule out small amounts of unreacted precursor salts (on TMV or on the substrate). We consider here especially FeCl_3 : its rather strong white line^{71,72} could account for the observed shift of the edge, but would go undetected in EDX (for % amounts). Air-oxidized Fe(II) species, too, can cause such shifts, and variations in XANES data.⁷² Based on this argument, the (small) difference in the oxidation states evaluated from edge and pre-edge features can be ascribed to the fact that the pre-edge peak is only sensitive to noncentrosymmetric positions. This is compatible with the presence of nonoxidic Fe cations, with centrosymmetric Fe positions.⁷³

The XANES data allow a further evaluation via extended X-ray absorption fine structure (EXAFS), which gives additional insight into structural features. This is especially useful in view of the near-amorphous nature of our oxide layers. Figure 8 shows the k^2 -weighted EXAFS functions $\chi(k)$ (k is the modulus of the photoelectron wave vector), and the Fourier transform (FT) functions, respectively, for mineralized TMV and for the references, which were recorded under identical conditions (see Experimental Section). The FT spectra feature peaks correspond to local atom correlations; their intensity is proportional to the number of neighbors. The modeling parameters for each atomic shell were bond distance (R), number of neighboring atoms at R , and Debye–Waller factors, which indicate structural site fluctuation and disorder. The

values were initially adjusted based on iron oxide references. The procedure yielded two distinct averaged distances, corresponding to Fe–O and Fe–Fe shells in the FT. The distances are similar for both references since they have very similar structures, and they fit to literature data.⁷⁴ The oscillations in both mineralized TMV samples (Figure 8 a) are similar to those of γ -Fe₂O₃ and Fe₃O₄, but diminished, as an amplitude envelope of the well-defined structures. This is due to the near-amorphous nature of the TMV Fe-oxide. We fitted the experimental data with theoretical signals relative to first and second shell contributions in the range of R=0.8–3.8 Å, considering average distances.⁷⁴ The Fe–O distances in Fe₃O₄ and Fe₂O₃ are 1.98 and 1.99 Å, respectively. For as-synthesized and annealed oxide on TMV we found 1.98 and 1.97 Å. The Fe–Fe distribution in spinel phases is more complex, since it comprises several distances corresponding to different cation occupations of the tetrahedral and octahedral positions (in the range of 2.96–3.70 Å). In our samples we observed an average of the Fe–Fe distances: 2.98 Å and 3.47 for the as-grown sample and 3.04 Å, and 3.50 for the annealed sample. This second shell (Fe–Fe) was less intense than the first shell, in contrast to the reference compounds. This can be attributed to the reduction of coordination for the Fe–Fe shell, a consequence of decreasing the size of the nanostructure, unlike bulk materials, where the coordination is higher.^{46,75} A rough fit of the Fe–Fe maxima indicates a very subtle increase in the number of neighbors in the annealed sample associated with the increment of order in the structure. Nevertheless, it is noteworthy that the increased crystallinity observed by XRD after annealing is not reflected in a substantial increase of coordination. Finite size effects discussed above may be masking this behavior. We should also take into account that the difference in the positions of the FT may also be due to the difference in occupation of

the tetrahedral and octahedral positions in the spinel references that can polarize the average distances values.⁷⁶

In summary, the local environment, although largely amorphous, shows some degree of order on the scale of the length of the Fe–O bonds. The direct iron environment can be compared to the situation in γ -Fe₂O₃, which is similar to that in Fe₃O₄. We find typical Fe–Fe and Fe–O distances, as in the crystalline bulk phases, since the relevant signals originate solely from the first neighboring atoms. By contrast, the disorder of the structure is related to size effects, and decreases the coordination in the outer shells. Both effects together we term the near-amorphous nature of our iron oxide, in agreement with our XRD and SAED data. As expected, annealing of this structure in air gives pure γ -Fe₂O₃,² and this process causes surprisingly few changes, despite the oxidation and the crystallization. Comparing XANES with EELS and XPS suggests that the latter indicate the presence of a fraction of Fe(II) in addition to Fe(III), while XANES points toward pure Fe(III). The shift of the edge observed by XANES may be due to the presence of iron cations in other states (comparable to FeCl₃ that contains Fe³⁺ ions), in addition to those in the oxides.

CONCLUSIONS

Iron oxide can be grown by a simple and mild solution technique on the rod-shaped plant virus TMV from a mixture of aqueous Fe(II) and Fe(III), which precipitates iron oxide on the exterior virus surface. We obtained a thin and continuous layer of ≈ 9 nm thickness, hence a nanotube, with a well-defined virus/oxide interface. Global and nanoscale diffraction suggests a near-amorphous nature for the oxide. Global and nanoscale

spectroscopy techniques prove the presence of a phase that is chemically similar to a mixture of the spinels magnetite (Fe_3O_4) and maghemite ($\gamma\text{-Fe}_2\text{O}_3$), meaning the presence of Fe(II) and Fe(III) in local tetrahedral and octahedral symmetry. Also the Fe–O distance of 1.98 Å is typical of the spinels, although here present in a near-amorphous oxide. The lack of crystallinity translates into a very weak magnetic moment; we found, however, a rather high coercivity. Its value of 0.04 T can be explained by the tubular structure of our iron oxide. Thermal treatment produced crystalline spinel phases with a much increased saturation magnetization of ≈ 1 emu/g, but with otherwise identical features, i.e., tubular shape and spectroscopical data. To the best of our knowledge, this is the first report in which iron oxide precipitated on a biotemplate has been investigated in such structural and chemical detail. Our mineralized TMV particles are magnetic, although with very small moments. It should be worthwhile to test their performance in ferrofluids, where their shape is expected to induce much larger viscosity changes than possible with spherical particles.⁵ In other words, the magnetic field would have a small influence in such applications, while the largest effect would be based on the unusual shape. The nanorod preparations may also serve as nontoxic models for the development of therapeutic approaches, based on the selective susceptibility of certain tumors to elongated nano-objects.^{30,81}

EXPERIMENTAL SECTION

Water (18 M/cm, < 10 ppb total organic content) was produced by a Milli-Q Advantage A10 (Millipore) fed with deionized water. TMV 0.1 mg/mL; diluted from stock suspensions in phosphate buffer kept at 4 °C, prepared according to Method A⁷⁷ was

dialyzed against water for 12 h; samples of 0.1 mL increased in volume by about 0.01 mL. Dialysis caps were Slide-A-Lyzer MINI Dialysis Units 100 kDa (Thermo Scientific). A premixed solution of 1 mM $(\text{NH}_4)_2\text{Fe}(\text{SO}_4)_2 \cdot 6\text{H}_2\text{O}$ (ACS Reagent 99%, Sigma-Aldrich) and 2 mM FeCl_3 (>97%, Sigma-Aldrich) was added, and the pH was adjusted to 9 by dropwise addition of 0.1 M NaOH (ACS-ISO, Panreac), yielding a brown precipitate. The reaction occurred just above $\text{pH} \approx 8$; but SEM images showed virtually no coating below $\text{pH} = 8.3$. The precipitation process took 10–12 min. Unless otherwise stated, all experiments were carried out at 300 K.

In order to check the nature of the mineralization reaction forming iron oxide (nanoparticles), we carried out the experiment first without virus, and then added TMV⁷⁷ (“post deposition”), under similar conditions as for the TMV mineralization: 0.01 mg/mL ToMV (chemically nearly identical to ToMV) was added with gentle pipet mixing into the reaction medium of Fe(II) and Fe(III) (see above). The pH was adjusted to 9 with 0.1 M NaOH, and stirred gently for 20 min with a pipet. Three microliter samples with and without viruses were taken (see Supporting Information).

Mineralized TMV particles were recovered by centrifugation and purified in a 100 kDa cutoff column (Amicon Ultra Centrifuge Filters, 0.5 mL, 100000 MWCO (molecular weight cutoff, Millipore) at 17530 g (14000 rpm, Eppendorf 5417C centrifuge) for 30 min. The particles were washed twice with ≈ 0.1 mL water. Additionally, remaining buffer salts and excess Fe(II) and Fe(III) were removed by dialysis against water for 4 h. Even after dialysis times of more than 12 and 24 h, the

particles did not change, and the coating of iron oxide was stable. The dialysis water was replaced twice, after <1 h, and after 2 h.

A Si(111) wafer ($>1 \Omega\text{cm}$, n-type doped with P) was cut with a dicer saw, without coating. The wafer pieces were rinsed with acetone, isopropanol, and water, dried with nitrogen, and treated for several seconds with an air plasma (PlasmaPen, PVATePla) to ensure a hydrophilic silicon oxide layer. A $1 \mu\text{L}$ droplet of purified mineralized TMV suspension was placed on a $4 \times 4 \text{ mm}$ silicon wafer piece, and dried in air.

For SEM we employed a FEI Quanta 250 (where also the EDX experiments were carried out), and a FEI Helios NanoLab, at high vacuum conditions, with various voltages (1–30 kV). Generally, 2–5 kV were ideal for imaging. For Figure 1 C we used a low acceleration voltage of 2 kV for EDX, in order to suppress the otherwise dominant silicon emission, and to increase surface sensitivity. TEM, EELS, and SAED data were obtained in a Cs-corrected 60 kV Titan G2 60–300 (FEI). EELS was calibrated with respect to the O 1s edge at 532 eV. Some samples were imaged at 200 kV (JEM-2100F, JEOL), or at 80 kV (JEM-1230, JEOL).

The magnetic properties of mineralized TMV particles were tested in a Quantum Design MPMS SQUID-VSM at 300 K. Most samples were investigated on B-doped silicon wafer pieces ($4 \times 4 \text{ mm}$) that had been washed with acetone, isopropanol and water. They were dried with a stream of nitrogen and treated for a few seconds with an air plasma pen (PVA TePla) operated at ambient pressure. We verified that these substrates gave purely diamagnetic signals. The mass of each clean piece was determined, a small volume ($\approx 1 \mu\text{L}$) of the mineralized TMV suspension was placed

close to the center and dried in air, after which the piece was weighed again to determine the mass of the mineralized TMV. The wafer piece was immobilized with diamagnetic glue to the MPMS quartz sample holder. The sample requires careful centering, depending on its shape and size (see Supporting Information S11).

The suspension of mineralized TMV was dropped on a glass slide and dried in air. The material was scraped off the glass slide onto a zero background silicon holder. The phases were identified in reflection mode in an X-ray diffractometer (X-Pert, Panalytical) with $\text{CuK}\alpha$ radiation (45 kV, 40 mA). Phase transformations were tested by treating the sample for 3 h in an oven at 520 K in air, as well as in vacuum at 570 K.

XPS spectra were recorded in a SAGE HR 100 system (SPECS, Germany) with soft X-rays of 1486.6 eV (Al anode). The binding energies were calibrated using the carbon C 1s peak at 284.8 eV. The spectra were measured with a pass energy of 30 eV. The XPS peaks were modeled with mixed Gaussian (30%)-Lorentzian (70%) curves.

XANES and EXAFS measurements at the Fe K-edge were performed at 300 K at the BM25 Spanish CRG Beamline (SpLine) of the ESRF (European Synchrotron Radiation Facility). A gas ionization chamber, filled with nitrogen and argon, was used to measure the incident beam intensity. The sample, deposited on a silicon substrate as detailed above, was placed in the beam path at 45° incidence. X-ray absorption was detected in fluorescence mode, measuring the emitted photons following X-ray absorption, using a 13 elements detector. Bulk metallic Fe, FeO, $\alpha\text{-Fe}_2\text{O}_3$, $\gamma\text{-Fe}_2\text{O}_3$, and Fe_3O_4 powders were also measured for comparison, but in transmission mode. As the sample amount available was very small, sample spectra were free of self-absorption

effects, while the larger mass of the reference substances modified the spectral profile in fluorescence. The proper procedure is thus to compare reference transmission spectra with the sample fluorescence spectrum. Data were normalized applying the same normalization parameters for all spectra by means of the Athena Software.⁷⁸

EXAFS data analysis was carried out with Athena to identify the starting point of the absorption edge, E_0 , and the pre-edge and postedge backgrounds. The software Viper⁷⁹ was used to process the normalized EXAFS signal $\chi(k)$ in the range of 2.5-12 Å⁻¹. The filtered signal (using a Hanning window) was theoretically recalculated, using amplitude and phase functions obtained by the FEFF code.⁸⁰

The Supporting Information is available free of charge on the ASC Publications website at DOI: 10.1021/acs.langmuir.5b04491.

(PDF)

AUTHOR INFORMATION

Corresponding Author

*E-mail: a.bittner@nanogune.eu

The authors declare no competing financial interest.

ACKNOWLEDGEMENTS

We are grateful to M. Möller (CIC biomaGUNE, San Sebastián) for additional TEM experiments (TMV/oxide samples, JEOL JEM-2100F). We thank M. Kobayashi for a sample of ToMV. We thank R. Zierold (Universität Hamburg) for valuable discussions. We thank Anadakumar Sarella (CIC nanoGUNE) for additional SQUID calibration data.

SS, AAK, AE, MAG, and AMB gratefully acknowledge financial support through the EU FP7 project “Magnifyco” (NMP4-SL-2009-228622). J.G.H. was funded by RIKEN. We acknowledge ESRF (Grenoble) for provision of synchrotron radiation facilities (project CH-3429), and the BM25-SpLine staff at ESRF for technical support and help far beyond their duties. We are grateful for financial support from the Spanish MECC and CSIC (PE-2010 6 0E 013), incl. provision of synchrotron radiation facilities, and also from the Spanish MINECO (MAT2010-16184), and from the Basque Government (PI2010-7 and Etortek). This work was partially supported by the Juan de la Cierva Program JCI-2010-07837. We thank FEI (Eindhoven, NL) for financial support.

REFERENCES

- (1) Falkenberg, G.; Fleissner, G.; Schuchardt, K.; Kuehbacher, M.; Thalau, P.; Mouritsen, H.; Heyers, D.; Wellenreuther, G.; Fleissner, G. Avian Magnetoreception: Elaborate Iron Mineral Containing Dendrites in the Upper Beak Seem to Be a Common Feature of Birds *PLoS One* **2010**, *5*, e9231.
- (2) Cornell, R. M. Schwertmann, U. The Iron Oxides: Structure, Properties, Reactions, Occurrences, and Uses; Wiley–VCH: Weinheim, Germany, 2006.
- (3) Faivre, D. In *Handbook of Biomineralization*; Editor, P. Behrens and E. Baeuerlein, Wiley–VCH Verlag GmbH: Weinheim, Germany, 2008.
- (4) Siponen, M. I.; Legrand, P.; Widdrat, M.; Jones, S. R.; Zhang, W.-J.; Chang, M. C. Y.; Faivre, D.; Arnoux, P.; Pignol, D. Structural insight into magnetochrome-mediated magnetite biomineralization. *Nature* **2013**, *502*, 681–684.
- (5) Wu, Z.; Mueller, A.; Degenhard, S.; Ruff, S. E.; Geiger, F.; Bittner, A. M.; Wege,

C.; Krill III, C. E. Enhancing the magnetoviscosity of ferrofluids by the addition of biological nanotubes. *ACS Nano* **2010**, *4*, 4531–4538.

(6) Zahr O. K.; Blum A. S. Solution phase gold nanorings on a viral protein template. *Nano. Lett.* **2012**, *12*, 2, 629–633.

(7) Balci, S.; Noda, K.; Bittner, A. M.; Kadri, A.; Wege, C.; Jeske, H.; Kern, K. Self-assembly of metal-virus nanodumbbells. *Angew. Chem., Int. Ed.* **2007**, *46*, 3149–3151.

(8) Knez, M.; Sumser, M.; Bittner, A. M.; Wege, C.; Jeske, H.; Martin, T. P.; Kern, K. Spatially selective nucleation of metal clusters on the tobacco mosaic virus. *Adv. Funct. Mater.* **2004**, *14*, 116–124.

(9) Górzny, M. Ł.; Walton, A. S.; Evans, S. D. Synthesis of High-Surface-Area Platinum Nanotubes Using a Viral Template. *Adv. Funct. Mater.* **2010**, *20*, 1295–1300.

(10) Lim, J.-S.; Kim, S.-M.; Lee, S.-Y.; Stach, E. A.; Culver, J. N.; Harris, M. T. Formation of Au/Pd Alloy Nanoparticles on TMV. *J. Nanomater.* **2010**, *2010*, 620505.

(11) Bromley, K. M.; Patil, A. J.; Perriman, A. W.; Stubbs, G.; Mann, S. Preparation of High Quality Nanowires by Tobacco Mosaic Virus Templating of Gold Nanoparticles. *J. Mater. Chem.* **2008**, *18*, 4796–4801.

(12) Wu, Z.; Zierold, R.; Mueller, A.; Ruff, S. E.; Ma, C.; Khan, A. A.; Geiger, F.; Sommer, B. A.; Knez, M.; Nielsch, K.; Bittner, A. M.; Wege, C.; Krill, C. E. Preparation and magnetoviscosity of nanotube ferrofluids by viral scaffolding and ALD on porous templates. *Phys. Status Solidi B* **2010**, *247*, 2412–2423.

(13) Royston, E.; Ghosh, A.; Kofinas, P.; Harris, M. T.; Culver, J. N. Self-assembly of virus-structured high surface area nanomaterials and their application as battery electrodes. *Langmuir* **2008**, *24*, 906–912.

- (14) Yang, C.; Manocchi, A. K.; Lee, B.; Yi, H. Viral templated palladium nanocatalysts for dichromate reduction. *Appl. Catal., B* **2010**, *93*, 282–291.
- (15) Balci, S.; Bittner, A. M.; Schirra, M.; Thonke, K.; Sauer, R.; Hahn, K.; Kadri, A.; Wege, C.; Jeske, H.; Kern, K. Catalytic coating of virus particles with zinc oxide. *Electrochim. Acta* **2009**, *54*, 5149–5154.
- (16) Fujikawa, S.; Kunitake, T. Surface Fabrication of Hollow Nanoarchitectures of Ultrathin Titania Layers from Assembled Latex Particles and Tobacco Mosaic Viruses as Templates. *Langmuir* **2003**, *19*, 6545–6552.
- (17) Shenton, W.; Douglas, T.; Young, M.; Stubbs, G.; Mann, S. Inorganic-Organic Nanotube Composites From Template Mineralization of Tobacco Mosaic Virus. *Adv. Mater.* **1999**, *11*, 253–256.
- (18) Shah, S. S.; Shah, S. N.; Heddle J. G Polymer-mediated Dual Mineralization of a Plant Virus: A Platinum Nanowire Encapsulated by Iron Oxide. *Chem. Lett.* **2015**, *44*, 79–81.
- (19) Laurent, S.; Forge, D.; Port, M.; Roch, A.; Robic, C.; Vander Elst, L.; Muller, R. N. Magnetic iron oxide nanoparticles: synthesis, stabilization, vectorization, physicochemical characterizations, and biological applications. *Chem. Rev.* **2008**, *108*, 2064–2110.
- (20) Wang, Y.; Yang, H. Synthesis of iron oxide nanorods and nanocubes in an imidazolium ionic liquid. *Chem. Eng. J.* **2009**, *147*, 71–78.
- (21) Ghosh D., Lee Y., Thomas S., Kohli A. G., Yun D. S., Belcher A. M., Kelly K. A. M13-templated magnetic nanoparticles for targeted in vivo imaging of prostate cancer. *Nat. Nanotechnol.* **2012**, *7*, 10, 677–682.

- (22) Beznosov S. N., Veluri P. S., Pyatibratov M. G., Chatterjee A., MacFarlane D. R., Fedorov O. V., Mitra S. Flagellar filament bio-templated inorganic oxide materials towards an efficient lithium battery anode. *Sci. Rep.* **2015**, *5*, 7736.
- (23) Almeida, T. P.; Fay, M. W.; Zhu, Y.; Brown, P. D. Hydrothermal growth mechanism of α -Fe₂O₃ nanorods derived by near in situ analysis. *Nanoscale* **2010**, *2*, 2390–2399.
- (24) Merchan-Merchan, W.; Saveliev, A. V.; Taylor, A. M. High rate flame synthesis of highly crystalline iron oxide nanorods. *Nanotechnology* **2008**, *19*, 125605.
- (25) Morber, J. R.; Ding, Y.; Haluska, M. S.; Li, Y.; Liu, J. P.; Wang, Z. L.; Snyder, R. L. PLD-Assisted VLS Growth of Aligned Ferrite Nanorods, Nanowires, and Nanobelts – Synthesis, and Properties. *J. Phys. Chem. B* **2006**, *110*, 21672–21679.
- (26) Wu, P.-C.; Wang, W.-S.; Huang, Y.-T.; Sheu, H.-S.; Lo, Y.-W.; Tsai, T.-L.; Shieh, D.-B.; Yeh, C.-S. Porous Iron Oxide Based Nanorods Developed as Delivery Nanocapsules. *Chem. Eur. J.* **2007**, *13*, 3878–3885.
- (27) Wu, M.-S.; Ou, Y.-H.; Lin, Y.-P. Electrodeposition of iron oxide nanorods on carbon nanofiber scaffolds as an anode material for lithium-ion batteries. *Electrochim. Acta* **2010**, *55*, 3240–3244.
- (28) Kumar, R. V.; Kolytyn, Y.; Xu, X. N.; Yeshurun, Y.; Gedanken, A.; Felner, I. Fabrication of magnetite nanorods by ultrasound irradiation. *J. Appl. Phys.* **2001**, *89*, 6324–6328.
- (29) Bødker, F.; Hansen, M. F.; Koch, C. B.; Lefmann, K.; Mørup, S. Magnetic

properties of hematite nanoparticles. *Phys. Rev. B* **2000**, *61*, 6826.

(30) Shukla S., Eber F. J., Nagarajan A. S., DiFranco N. A., Schmidt N., Wen A. M., Eiben S., Twyman R. M., Wege C., Steinmetz N. F. The Impact of Aspect Ratio on the Biodistribution and Tumor Homing of Rigid Soft-Matter Nanorods. *Adv. Healthcare Mater.* **2015** *22*, 874–82.

(31) Kim, C. H.; Chun, H. J.; Kim, D. S.; Kim, S. Y.; Park, J.; Moon, J. Y.; Lee, G.; Yoon, J.; Jo, Y.; Jung, M.-H.; Jung, S. I.; Lee, C. J. Magnetic anisotropy of vertically aligned α -Fe₂O₃ nanowire array. *Appl. Phys. Lett.* **2006**, *89* (22), 223103.

(32) Lin, M. M.; Kim, H.-H.; Kim, H.; Muhammed, M.; Kim, D. K. Iron oxide-based nanomagnets in nanomedicine: fabrication and applications. *Nano Rev.* **2010**, *1*, 4883.

(33) Bigall, N. C.; Dilella, E.; Dorfs, D.; Beoutis, M.-L.; Pugliese, G.; Wilhelm, C.; Gazeau, F.; Khan, A. A.; Bittner, A. M.; Garcia, M. A.; Garcia-Hernandez, M.; Manna, L.; Pellegrino, T. Hollow Iron Oxide Nanoparticles in Polymer Nanobeads as MRI Contrast Agents. *J. Phys. Chem. C* **2015**, *119*, (11), 6246–6253.

(34) Tai, Y.; Wang, L.; Yan, G.; Gao, J.-m.; Yu, H.; Zhang, L. Recent research progress on the preparation and application of magnetic nanospheres. *Polym. Int.* **2011**, *60*, 976–994.

(35) Durán, J. D. G.; Arias, J. L.; Gallardo, V.; Delgado, A. V. Magnetic colloids as drug vehicles. *J. Pharm. Sci.* **2008**, *97*, 2948–2983.

(36) Gupta, A. K.; Gupta, M. Synthesis and surface engineering of iron oxide nanoparticles for biomedical applications. *Biomaterials* **2005**, *26*, 3995–4021.

(37) Liu, C.; Chung, S.-H.; Jin, Q.; Sutton, A.; Yan, F.; Hoffmann, A.; Kay, B. K.; Bader, S. D.; Makowski, L.; Chen, L. Magnetic viruses via nano-capsid templates. *J.*

Magn. Magn. Mater. **2006**, *302*, 47–51.

(38) Balci, S.; Leinberger, D. M.; Knez, M.; Bittner, A. M.; Boes, F.; Kadri, A.; Wege, C.; Jeske, H.; Kern, K. Printing and Aligning Mesoscale Patterns of Tobacco mosaic virus on Surfaces. *Adv. Mater.* **2008**, *20*, 2195–2200.

(39) Kobayashi, M.; Seki, M.; Tabata, H.; Watanabe, Y.; Yamashita, I. Fabrication of Magnetic Nanoparticles Using Tobamoviruses. *Nano Lett.* **2010**, *10*, 773–776.

(40) Tsukamoto, R.; Muraoka, M.; Seki, M.; Tabata, H.; Yamashita, I. Synthesis of CoPt and FePt₃ Nanowires Using the Central Channel of Tobacco Mosaic Virus as a Biotemplate. *Chem. Mater.* **2007**, *19*, 2389–2391.

(41) Altintoprak K., Seidenstücker A., Welle A., Eiben S., Atanasova P., Stitz N., Plettl A., Bill J., Gliemann H., Jeske H., Rothenstein D., Geiger F., Wege C. Peptide-equipped tobacco mosaic virus templates for selective and controllable biomineral deposition. *Beilstein J. Nanotechnol.* **2015** *6*, 1399–1412.

(42) Mehta, R. V.; Upadhyay, R. V.; Charles, S. W.; Ramchand, C. N. Direct binding of protein to magnetic particles. *Biotechnol. Tech.* **1997**, *11*, 493–496.

(43) Alonso, J. M.; Górzny, M. Ł.; Bittner, A. M. The physics of tobacco mosaic virus and virus-based devices in biotechnology. *Trends Biotechnol.* **2013**, *31*, 530–538.

(44) Baumgartner, J.; Antonietta Carillo, M.; Eckes, K. M.; Werner, P.; Faivre, D. Biomimetic Magnetite Formation: From Biocombinatorial Approaches to Mineralization Effects. *Langmuir* **2014**, *30*, 2129–2136.

(45) Faivre, D.; Schüler, D. Magnetotactic Bacteria and Magnetosomes. *Chem. Rev.* **2008**, *108*, 4875–4898.

(46) Machala, L.; Zboril, R.; Gedanken, A. Amorphous Iron(III) Oxide-A Review. *J.*

Phys. Chem. B **2007**, *111*, 4003–4018.

(47) Cao, X.; Prozorov, R.; Kolytyn, Y.; Kataby, G.; Felner, I.; Gedanken, A. Preparation of amorphous Fe₂O₃ powder with different particle sizes. *J. Mater. Chem.* **1997**, *7*, 2447–2451.

(48) Phu, N. D.; Ngo, D. T.; Hoang, L. H.; Luong, N. H.; Chau, N.; Hai, N. H. Crystallization process and magnetic properties of amorphous iron oxide nanoparticles. *J. Phys. D: Appl. Phys.* **2011**, *44*, 345002.

(49) Wang, C.; Baer, D. R.; Amonette, J. E.; Engelhard, M. H.; Antony, J.; Qiang, Y. Morphology and Electronic Structure of the Oxide Shell on the Surface of Iron Nanoparticles. *J. Am. Chem. Soc.* **2009**, *131*, 8824–8832.

(50) Palchik, O.; Felner, I.; Kataby, G.; Gedanken, A. Amorphous iron oxide prepared by microwave heating. *J. Mater. Res.* **2000**, *15*, 2176–2181.

(51) Liao, X.; Zhu, J.; Zhong, W.; Chen, H.-Y. Synthesis of amorphous Fe₂O₃ nanoparticles by microwave irradiation. *Mater. Lett.* **2001**, *50*, 341–346.

(52) Ayyub, P.; Multani, M.; Barma, M.; Palkar, V. R.; Vijayaraghavan, R. Size-induced structural phase transitions and hyperfine properties of microcrystalline Fe₂O₃. *J. Phys. C: Solid State Phys.* **1988**, *21*, 2229–2245.

(53) Hurt, D.; Shi, L.; Amann, A. Versatile SQUID Susceptometer With Multiple Measurement Modes. *IEEE Trans. Magn.* **2013**, *49*, 3541–3544.

(54) Zhang, Y. C.; Tang, J. Y.; Hu, X. Y. Controllable synthesis and magnetic properties of pure hematite and maghemite nanocrystals from a molecular precursor. *J. Alloys Compd.* **2008**, *462*, 24–28.

(55) Lu, H. M.; Zheng, W. T.; Jiang, Q. Saturation magnetization of ferromagnetic and

- ferromagnetic nanocrystals at room temperature. *J. Phys. D: Appl. Phys.* **2007**, *40*, 320–325.
- (56) Qu, X.; Kobayashi, N.; Komatsu, T. Solid Nanotubes Comprising α -Fe₂O₃ Nanoparticles Prepared from Ferritin Protein. *ACS Nano*. **2010**, *4*, 1732–1738.
- (57) Bachmann, J.; Jing, K.; Knez, M.; Barth, S.; Shen, H.; Mathur, S.; Gösele, U.; Nielsch, K. Ordered Iron Oxide Nanotube Arrays of Controlled Geometry and Tunable Magnetism by Atomic Layer Deposition. *J. Am. Chem. Soc.* **2007**, *129*, 9554–9555.
- (58) Suber, L.; Imperatori, P.; Ausanio, G.; Fabbri, F.; Hofmeister, H. Synthesis, Morphology, and Magnetic Characterization of Iron Oxide Nanowires and Nanotubes. *J. Phys. Chem. B* **2005**, *109*, 7103–7109.
- (59) Geng, B.; Zhan, F.; Jiang, H.; Guo, Y.; Xing, Z. Egg albumin as a nanoreactor for growing single-crystalline Fe₃O₄ nanotubes with high yields. *Chem. Commun.* **2008**, 5773–5775.
- (60) Zhou, S. M.; Zhang, X. T.; Gong, H. C.; Zhang, B.; Wu, Z. S.; Du, Z. L.; Wu, S. X. Magnetic enhancement of pure gamma Fe₂O₃ nanochains by chemical vapour deposition. *J. Phys.: Condens. Matter.* **2008**, *20*, 075217.
- (61) Park, S.-J.; Kim, S.; Lee, S.; Khim, Z. G.; Char, K.; Hyeon, T. Synthesis and Magnetic Studies of Uniform Iron Nanorods and Nanospheres. *J. Am. Chem. Soc.* **2000**, *122*, 8581-8582.
- (62) Xue, D. S.; Shi, H. G. The fabrication and characteristic properties of amorphous Fe_{1-x}P_x alloy nanowire arrays. *Nanotechnology*. **2004**, *15*, 1752–1755.
- (63) Ennas, G.; Musinu, A.; Piccaluga, G.; Zedda, D.; Gatteschi, D.; Sangregorio, C.; Stanger, J. L.; Concas, G.; Spano, G. Characterization of Iron Oxide Nanoparticles in an

Fe₂O₃–SiO₂ Composite Prepared by a Sol–Gel Method. *Chem. Mater.* **1998**, *10*, 495–502.

(64) Han, Q.; Liu, Z.; Xu, Y.; Chen, Z.; Wang, T.; Zhang, H. Growth and Properties of Single-Crystalline γ -Fe₂O₃ Nanowires. *J. Phys. Chem. C* **2007**, *111*, 5034–5038.

(65) Geng, B. Y.; Ma, J. Z.; Liu, X. W.; Du, Q. B.; Kong, M. G.; Zhang, L. D. Hydrophilic polymer assisted synthesis of room-temperature ferromagnetic Fe₃O₄ nanochains. *Appl. Phys. Lett.* **2007**, *90*, 043120.

(66) Zhang, Y.; Liu, J.-Y.; Ma, S.; Zhang, Y.-J.; Zhao, X.; Zhang, X.-D.; Zhang, Z.-D. Synthesis of PVP-coated ultra-small Fe₃O₄ nanoparticles as a MRI contrast agent. *J. Mater. Sci.: Mater. Med.* **2010**, *21*, 1205–1210.

(67) Lin, T.-C.; Seshadri, G.; Kelber, J. A. A consistent method for quantitative XPS peakanalysis of thin oxide films on clean polycrystalline iron surfaces. *Appl. Surf. Sci.* **1997**, *119*, 83–92.

(68) Brundle, C. R.; Chuang, T. J.; Wandelt, K. Core and valence level photoemission studies of iron oxide surfaces and the oxidation of iron. *Surf. Sci.* **1977**, *68*, 459–468.

(69) Yamashita, T.; Hayes, P. Analysis of XPS spectra of Fe²⁺ and Fe³⁺ ions in oxide materials. *Appl. Surf. Sci.* **2008**, *254*, 2441–2449.

(70) Corrias, A.; Mountjoy, G.; Loche, D.; Puentes, V.; Falqui, A.; Zanella, M.; Parak, W. J.; Casula, M. F. Identifying Spinel Phases in Nearly Monodisperse Iron Oxide Colloidal Nanocrystal. *J. Phys. Chem. C* **2009**, *113*, 18667–18675.

(71) Manceau, A.; Gates, W. P. Surface Structural Model for Ferrihydrite. *Clays Clay Miner.* **1997**, *45*, 448–460.

(72) Kanngießer, B.; Hahn, O.; Wilke, M.; Nekat, B.; Malzer, W.; Erko, A.

Investigation of oxidation and migration processes of inorganic compounds in ink-corroded manuscripts. *Spectrochim. Acta B* **2004**, *59*, 1511–1516.

(73) Ballirano, P.; Belardi, G. Rietveld refinement of the Tutton salt

$\text{K}_2[\text{Fe}(\text{H}_2\text{O})_6](\text{SO}_4)_2$. *Acta Crystallogr., Sect. E: Struct. Rep. Online* **2006**, *62*, i58–i60.

(74) Signorini, L.; Pasquini, L.; Savini, L.; Carboni, R.; Boscherini, F.; Bonetti, E.; Giglia, A.; Pedio, M.; Mahne, N.; Nannarone, S. Size-dependent oxidation in iron/iron oxide core-shell nanoparticles. *Phys. Rev. B* **2003**, *68*, 195423.

(75) Khanh, B. T. H. L.; Hoang, V. V.; Zung, H. Structural properties of amorphous Fe_2O_3 nanoparticles. *Eur. Phys. J. D* **2008**, *49*, 325–332.

(76) Carta, D.; Casula, M. F.; Mountjoy, G.; Corrias, A. Formation and cation distribution in supported manganese ferrite nanoparticles: an X-ray absorption study.

Phys. Chem. Chem. Phys. **2008**, *10*, 3108–3117.

(77) Kadri, A.; Maiß, E.; Amsharov, N.; Bittner, A. M.; Balci, S.; Kern, K.; Jeske, H.; Wege, C. Engineered Tobacco mosaic virus mutants with distinct physical characteristics in planta and enhanced metallization properties. *Virus Res.* **2011**, *157*, 35–46.

(78) Newville, M. IFEFFIT: interactive XAFS analysis and FEFF fitting. *J. Synchrotron Radiat.* **2001**, *8*, 322–324.

(79) Klementev, K. V. Extraction of the fine structure from x-ray absorption spectra. *J. Phys. D: Appl. Phys.* **2001**, *34*, 209–217.

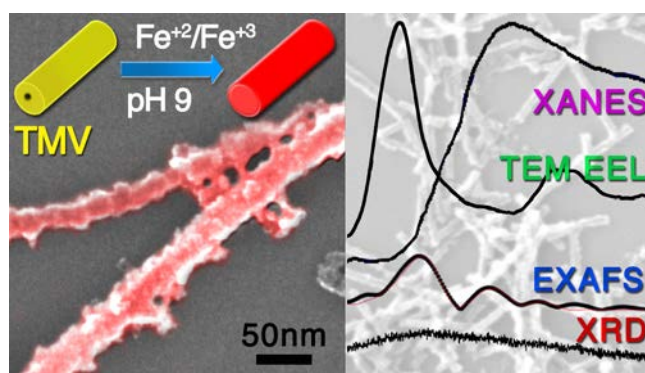
(80) Rehr, J. J. Recent Developments in Multiple-Scattering Calculations of XAFS and XANES. *Jpn. J. Appl. Phys.* **1993**, *32*, 8–12.

(81) Geng, Y.; Dalhaimer, P.; Cai, S.; Tsai, R.; Tewari, M.; Minko, T.; Discher, D. E. Shape effects of filaments versus spherical particles in flow and drug delivery. *Nat.*

Nanotechnol. **2007**, 2, 249–255.

For Table of Contents :

Virus-Templated Near-Amorphous Iron Oxide Nanotubes



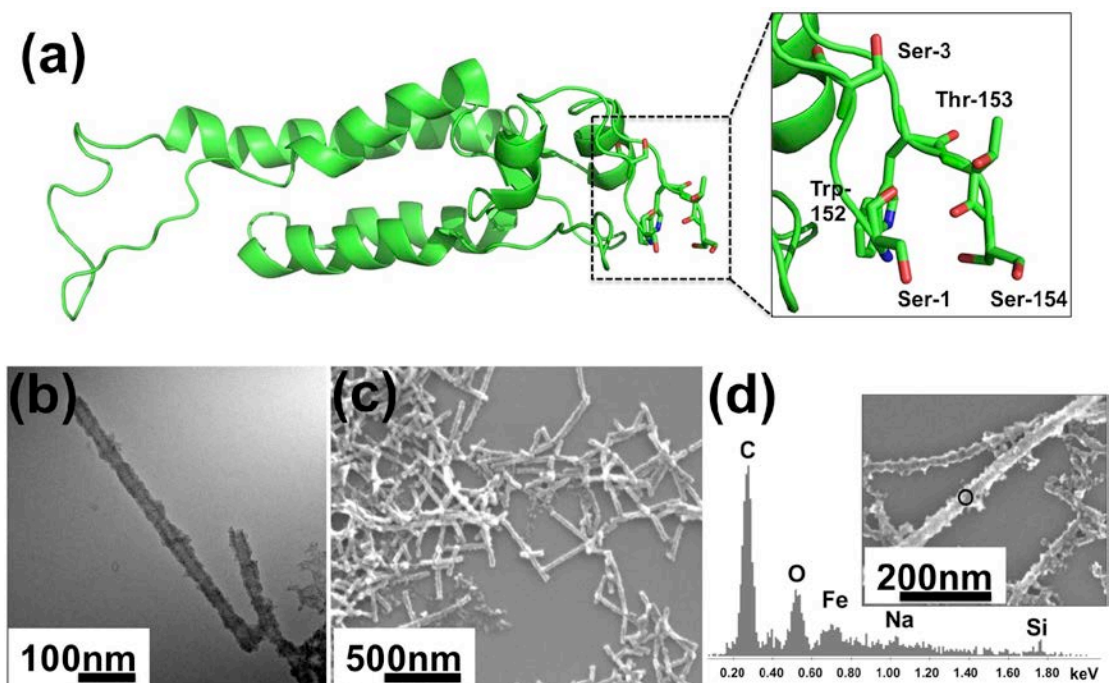


Figure 1. (a) Cartoon model of one of 2103 coat proteins of TMV (pdb 2TMV). The leftmost part clads the internal channel, the middle part is a rather rigid four-helix bundle, and the rightmost part forms the external surface. Residues 1, 3, and 152–154 are on the right and shown as stick models. The terminal nitrogen and the exposed indole nitrogen are shown in blue while the exposed oxygens are shown in red. The pdb model does not include the last four residues, C-terminal to residue 155, which are rather flexible. They contain another hydroxyl group (Thr-158) and the carboxylate terminus. The inset shows a magnification of the region of interest with relevant amino acids labeled. The Figure was produced using PyMOL (see Experimental Section). (b) TEM image of two linearly assembled TMVs mineralized with a mixture of Fe(II) and Fe(III); another slightly bent virion can be seen in the right of the image. The virions (light gray) are homogeneously coated (black), and the TMV/mineral interface is very smooth. (c) SEM image shows virions homogeneously coated by iron oxide (light gray) and forming a grid-like irregular network. (d) EDX spectrum showing the presence of iron on mineralized TMV. The silicon and oxygen signals stem mainly from the wafer substrate. Inset: SEM image; the spot from which the EDX spectrum was recorded, marked by a circle.

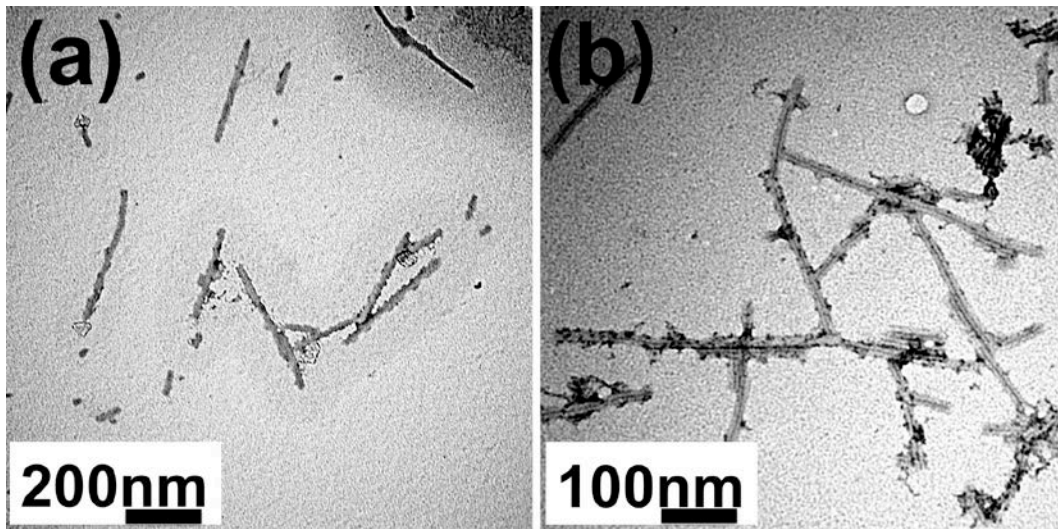


Figure 2. Unpurified ToMV after addition to a mixture of Fe(II) / Fe(III) at pH 9 (post mineralization conditions). (a) TEM image without negative stain shows ToMV (gray color rods) with sparse deposition of iron oxide. (b) The same sample after staining with 2% phosphotungstate. The virions show the 4 nm inner channel (black) with sparse, random deposition of iron oxide.

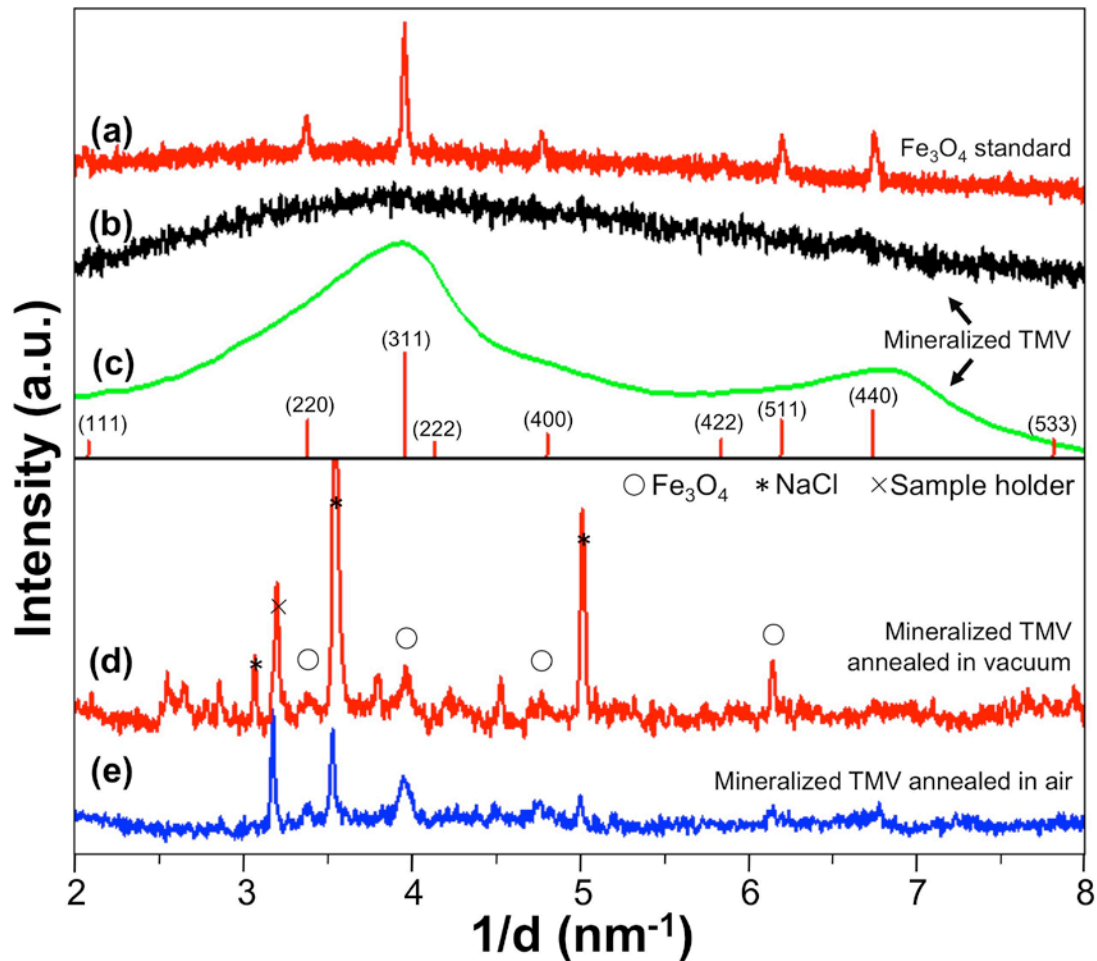


Figure 3. Diffraction experiments; for simplicity, all peak assignments are based on the Fe_3O_4 structure. (a) XRD from Fe_3O_4 standard (powder) of mass 3.5 mg; (b) from iron oxide-mineralized TMV (mass 5.2 mg) showing a broad maximum at the (311) position; both on a zero background holder. (c) Radial profile of SAED pattern (for original SAED pattern see Supporting Information) of mineralized TMV, showing two broad maxima at the (311) and (440) positions, and shoulders at (400) and (511). (d) Mineralized TMV after annealing in vacuum to 570 K, and (e) after annealing in air to 520 K. Additional peaks correspond to NaCl from the educts in the synthesis.

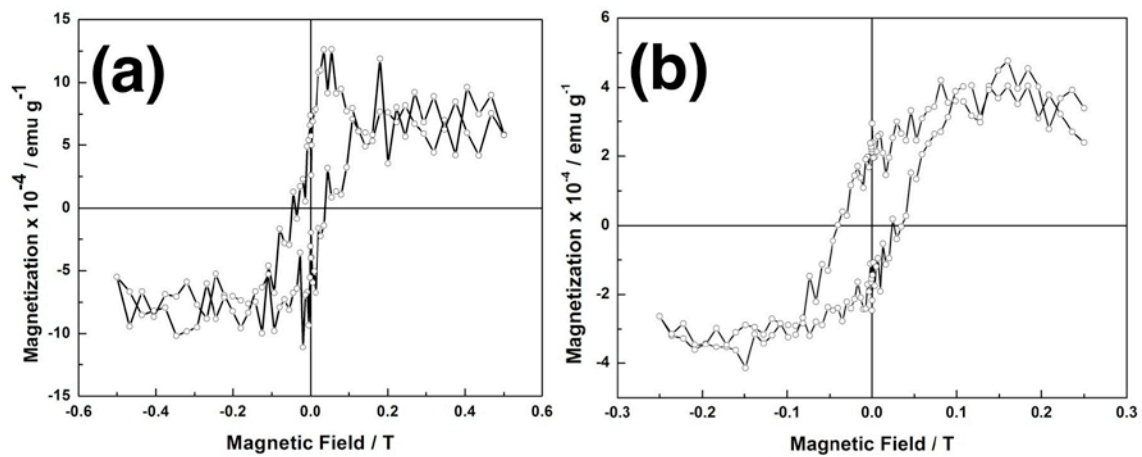


Figure 4. (a) Magnetization curve for mineralized TMV at 300 K. (b) Magnetization curve for mineralized TMV at 5 K.

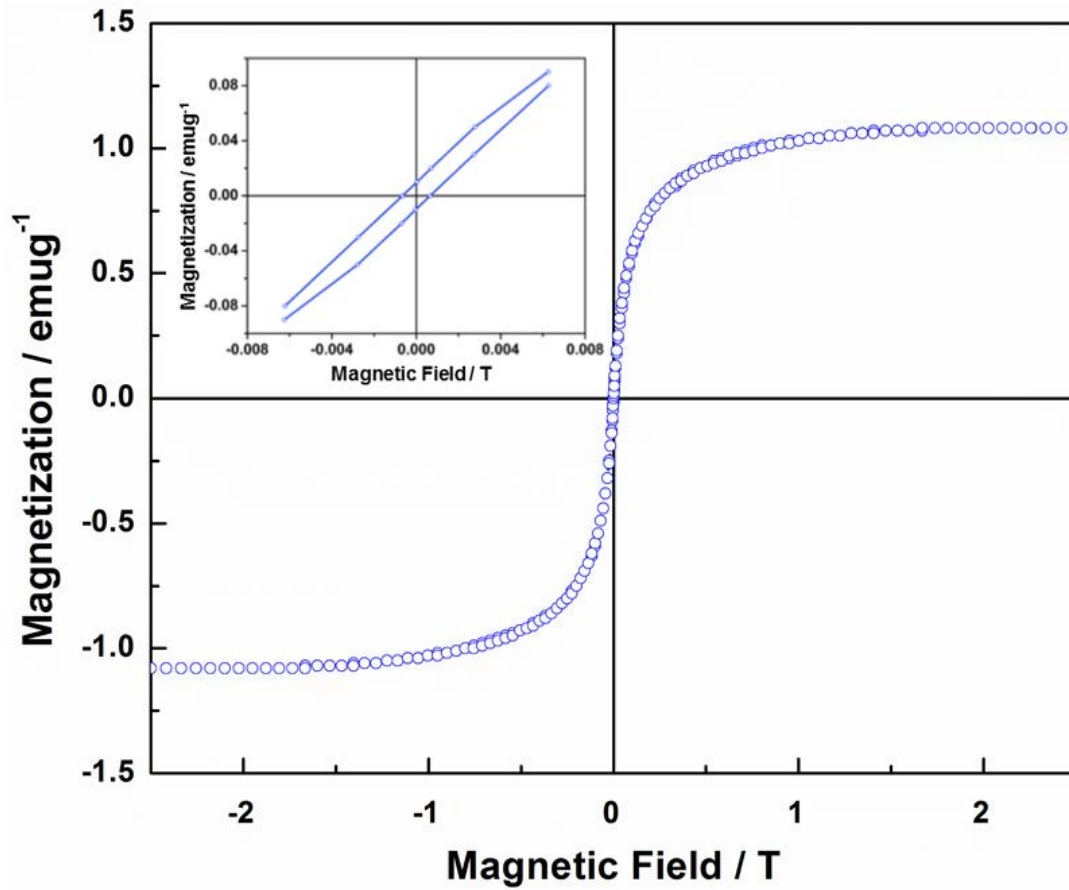


Figure 5. Magnetization curve (at 300 K) for mineralized TMV after heating in air to 520 K. A detail of the low field region is shown in the inset.

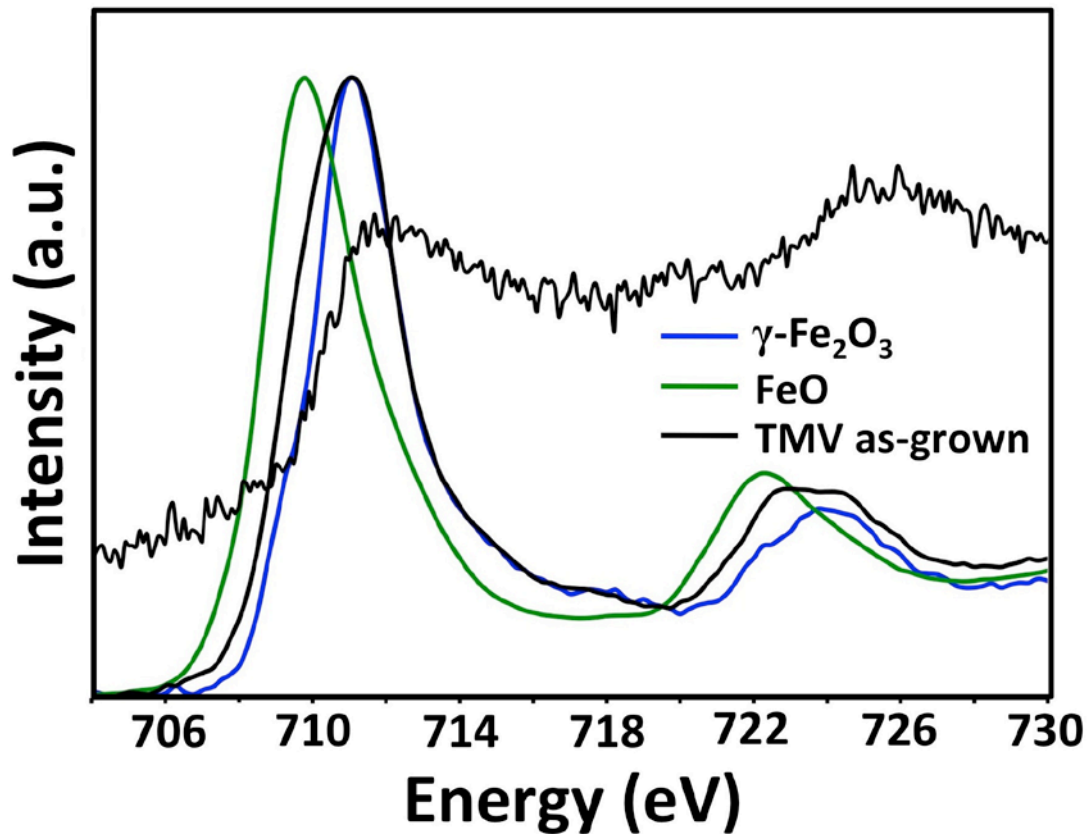


Figure. 6. TEM EELS and XPS from sample (black) and reference compounds (colored) in the Fe 3p region (Fe L edge). Black: EELS from TMV/iron oxide; blue: EELS from γ -Fe₂O₃, green: from FeO standard, recorded under identical TEM conditions. Noisy trace: XPS of mineralized TMV, purified sample.

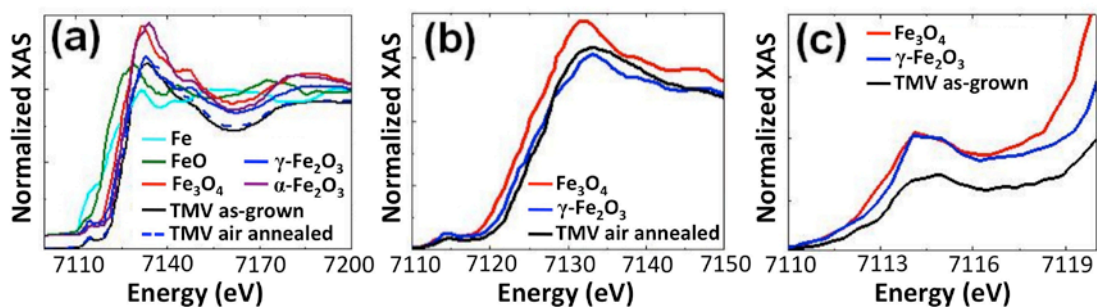


Figure 7. (a) XANES spectra measured at the Fe K-edge for mineralized TMV and the reference compounds. (b) Detail of the XANES spectra at the Fe K-edge region for mineralized and air annealed TMV, and for bulk Fe₃O₄ and γ-Fe₂O₃ as reference standards. (c) The XANES spectra at the Fe K pre-edge region for mineralized TMV compared with bulk Fe₃O₄ and γ-Fe₂O₃ as reference standards.

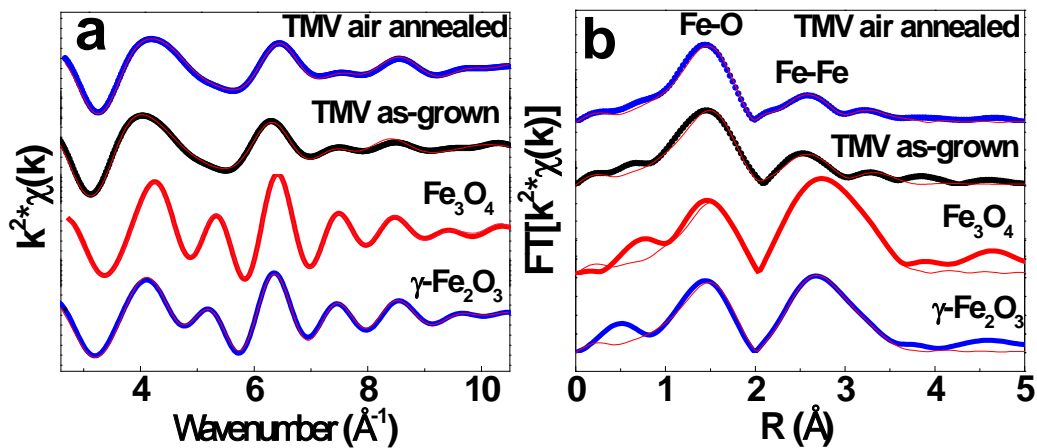


Figure 8. EXAFS from the Fe K edge for the reference standards Fe_3O_4 and $\gamma\text{-Fe}_2\text{O}_3$, and for mineralized and air annealed TMV. (a) k^2 -weighted EXAFS functions ($\chi(k) \cdot k^2$), (b) Fourier transforms.

For Table of Contents:

Virus-Templated Near-Amorphous Iron Oxide Nanotubes

